Advances in Applied Mathematics and Mechanics
Adv. Appl. Math. Mech., Vol. **2**, No. 5, pp. 587-608

DOI: 10.4208/aamm.10-10S05
October 2010

Some Advances in Applications of Lattice Boltzmann Method for Complex Thermal Flows

Ridha Djebali[1,*], Habib Sammouda[1] and Mohammed El Ganaoui[2]

[1] *University of Tunis El-Manar, FS of Tunis, Department of Physics, LETTM, 1060 Tunis, Tunisia*
[2] *CNRS/SPCTS, UMR 6638, FST of Limoges, Department of Physics, 87060 Limoges, France*

Received 16 March 2010; Accepted (in revised version) 21 April 2010

Available online 13 July 2010

Abstract. Over the past two decades, there have been enormous advances in lattice Boltzmann (LB) numerical simulation and modelling. The lattice Boltzmann method has become a practical and promising tool for many fluid problems. A majority of recent studies have relied on numerical computations of isothermal flows. However, much less efforts have been devoted to complex thermal flows, such as flows in porous media subjected to external magnetic force, flows with temperature-dependent properties. In this paper, an overview is made based on some accomplishments in these numerical endeavours. Along with the paper's sections, the state-of-the-art trend and the LBM advances in modelling and in computational aspects for specific classes of problems of major interest will be fully touched on. Concluding remarks are given and the axis of our future studies will be traced.

AMS subject classifications: 76M28, 70K50, 76S05, 82D10

Key words: LB method, Bifurcations and instability, porous media flows, plasma jets.

1 Introduction

Over the past two decades, the lattice Boltzmann method (LBM) has been widely adopted to solve linear and nonlinear partial differential equations (such as Burger's equation, wave equation, Poisson equation etc.) and progressively the method shows its efficiency, to offer today a powerful tool for simulating fluid flows [1–4]. Unlike the conventional Computational Fluid Dynamics (CFD) ones based on continuum mechanics, the method starts from mesoscopic kinetic equation and statistical physics

*Corresponding author.
URL: `http://www.unilim.fr/spcts/-Doctorants-.html`
Email: ridha.djebali@etu.unilim.fr (R. Djebali), habib.sammouda@fsm.rnu.tn (H. Sammouda), ganaoui@unilim.fr (M. El Ganaoui)

(the Boltzmann equation) and determines the macroscopic quantities (density, velocity, pressure etc.). In the framework of the LBM, the lattice Boltzmann equation is time and space-discretized and a set of density distribution functions (corresponding to fictitious particles that colloid and stream) are stored at each lattice node. The updating mechanism consists of two steps: a streaming along a set of discrete velocities and a relaxation equivalent to the collision frequency of particles. In the LBM, the macroscopic quantities are locally computed by using each time step's density distribution functions. The pressure derives from the density via an equation of state. The solution procedure of the method provides many advantages resulting in simpler set of equations (resulting in algebraic operations unlike algebraic equations for classical CFD methods), parallel computations, easy handling of complex geometries, easy handling of coupling equations by simply adding force/sink term in discretized equation.

For instance, the LBM presents the features of simulating classical flows [5–9], flow with complex geometries [10], multiphase flows [11, 12], multicomponent flows [13], it overcomes some shortcomings of classical CFD methods (discretization, CFL stability condition, $\cdots$,) and enables us to investigate time-dependent flow transition more conveniently since its remarkable capability in recording transients of flow development. Moreover, previous LB based works almost used Cartesian coordinates system and focused the interest on steady state flows. Some recent works have attempted the fully unsteady flow regimes [14, 15] and other coordinate systems [16–19]. However, a fully LB-understanding of transition thresholds is less considered in the literatures although the occurring phenomena are of practical interest in industry [20], such as for crystal growth in low Prandtl number flows. Furthermore, very high temperature flows such as plasma jets (where all diffusion parameters are temperature dependent), free jet flows (where special attention is made for boundary condition treatment) and porous media flows under magnetic force (where the forcing term needs special treatment), are of practical and scientific interest and were not yet (or few) approached by the LBM at our knowledge. Since these topics are of vital importance in numerous applications, the present work is devoted to review our knowledge for recent improvement and progress in its modelling and simulation using the LBM.

The present works is organized as follows: the introduction section presents the basic concept of the LBM and its implementation for thermal flows; the validation section provides several investigations of steady and unsteady natural convection flows with qualitative and quantitative comparisons with previous numerical results. The last section is devoted to review some recent progress in LB simulation and modelling of some complex thermal flows, namely low Prandtl number fluid melts flows subject to symmetry breaking and transition to unsteady regimes, plasma jets flows for pure gas and gases mixture and flows in porous media subject to external magnetic force. For the three examples, the focus is put on the advances in LB modelling and the predictability level in the results rather than to describe the models in detail. Comparisons with previous results using classical CFD methods are given in all cases for model validation.

2 Method of solution: outlines of LB thermal models

The Boltzmann equation derived from Statistical Physics describes the probability of existence (in term of distribution function f) of a particle at the time t in the location $\vec{x}$ and with a velocity $\vec{v}$

$$\frac{\partial f}{\partial t} + \vec{\zeta}\frac{\partial f}{\partial \vec{x}} + \frac{\partial f}{\partial \vec{\zeta}}\vec{F} = \Omega(f), \tag{2.1}$$

where $\vec{F}$ is an external force and the operator $\Omega(f)$ describes the particles interactions following the collision process. Then the time evolution of the distribution function f is governed by the advection term $\vec{\zeta}(\partial f/\partial \vec{x})$, the external force term $(\partial f/\partial \vec{\zeta})\vec{F}$ and the collision term $\Omega(f)$.

The Bhatnagar-Gross-Krook (BGK) model assumes that the distribution function f relaxes towards the Maxwellian distribution f^{eq} in an average relaxation time τ related to the time between two particle-collisions

$$\Omega(f) = \frac{1}{\tau_f}(f_k^{eq} - f_k), \tag{2.2}$$

the relaxation time τ controls the rate towards equilibrium from the non-equilibrium state and the equilibrium distribution function is chosen to be an expansion in the velocity and to ensure that the conservation laws are obeyed.

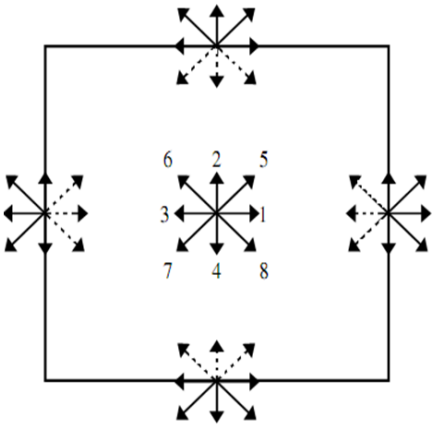

Figure 1: The 9-bits LB model and domain boundaries treatment: solid line (known distributions) and dotted-lines (unknown distributions).

The lattice Boltzmann of the Eq. (2.1) is discretized and assumed valid along specific directions of linkages (see Fig. 1). Then the discrete Boltzmann equation is replaced by its discrete functions f_k as

$$\frac{\partial f_k}{\partial t} + e_{ki}\frac{\partial f_k}{\partial x_i} + \frac{\partial f_k^{eq}}{\partial e_{ki}}F_i \approx \frac{1}{\tau_f}(f_k^{eq} - f_k), \tag{2.3}$$

where the indices k and i describe the directions of linkages and the Cartesian coordinates components respectively. The general form of the Boltzmann equation following a time and space finite difference discretization and assuming equals the time and space steps $\Delta x = \Delta t$ is written as

$$f_k(\vec{x}+\vec{e}_k\Delta t, t+\Delta t) = f_k(\vec{x},t) + \frac{\Delta t}{\tau_f}\left(f_k^{eq}(\vec{x},t) - f_k(\vec{x},t)\right) + \Delta t F_k, \tag{2.4}$$

where

$$F_k = \frac{\vec{F}(\vec{e}_k - \vec{u})f_k^{eq}}{RT_0},$$

with R=1 in LB modelling and T_0 is determined by the LB model (e.g., T_0=1/3 in D2Q9 or D2Q19 models). This equation is used for numerical simulations and determines the time evolution of the density distribution function f. The time evolution of Eq. (2.4) is solved in two steps, i.e., the so-called collision-streaming process

$$\widetilde{f}_k(\vec{x},t) = f_k(\vec{x},t) + \frac{\Delta t}{\tau_f}\left(f_k^{eq}(\vec{x},t) - f_k(\vec{x},t)\right) + \Delta t F_k, \tag{2.5a}$$

$$f_k(\vec{x}+\vec{e}_k\Delta t, t+\Delta t) = \widetilde{f}_k(\vec{x},t). \tag{2.5b}$$

The Navier-Stokes equations are second-order nonlinear equations in velocity. Therefore, the equilibrium distribution function must be expressed in $\mathcal{O}(u^2)$ form; it also depends on the type of problem-solving. For a 2D problem flow, with 9-bits model, the equilibrium distribution function, after some derivation $\big($expansion of the Maxwellian distribution and neglecting terms of $\mathcal{O}(u^2)\big)$ is written as

$$f_k^{eq} = w_k\rho\Big[1 + 3(\vec{e}_k\cdot\vec{u}) + \frac{9}{2}(\vec{e}_k\cdot\vec{u})^2 - \frac{3}{2}(\vec{u}\cdot\vec{u})^2\Big], \tag{2.6}$$

where w_k=4/9 for k=0; w_k=1/9 for k=1, $\cdots$,4; w_k=1/36 for k=5, $\cdots$,8, $|\vec{e}_k|$=1 along the axis and $|\vec{e}_k|$=$\sqrt{2}$ along the diagonals.

When a thermal flow is considered, the distribution function g for the temperature fields obeys the same formulation discussed above and its evolution equation (without heat loss/generation) is

$$g_k(\vec{x}+\vec{e}_k\Delta t, t+\Delta t) = g_k(\vec{x},t) + \frac{\Delta t}{\tau_g}\left(g_k^{eq}(\vec{x},t) - g_k(\vec{x},t)\right). \tag{2.7}$$

Two thermal models are considered in this study, i.e., the internal energy distribution model (model I) [8] and the passive scalar model (model II) [21]. For the internal energy distribution model, the equilibrium distribution (in 9-bits model) is written as:

$$g_k^{eq} = \omega_k\rho\varepsilon\Big[\frac{3}{2}(\vec{e}_k^2 - \vec{u}^2) + 3\Big(\frac{3}{2}\vec{e}_k^2 - 1\Big)(\vec{e}_k\cdot\vec{u}) + \frac{9}{2}(\vec{e}_k\cdot\vec{u})^2\Big]. \tag{2.8}$$

For the passive scalar approach, the equilibrium part (in 4-bits model) is written as:

$$g_k^{eq} = \frac{1}{4}\varepsilon\Big[1 + 2(\vec{e}_k \cdot \vec{u})\Big], \tag{2.9}$$

where $\varepsilon \equiv T$ is the dimensionless temperature field. In a comparison study (not presented here), we have shown that the two models have the same features in terms of accuracy and iterations numbers needed for convergence. In general, both the two approaches recover the energy equation.

The macroscopic flow properties (density, velocity, temperature) are obtained by collecting the distribution functions over the discrete velocities at each node site as:

$$\rho = \sum_{k=0,8} f_k, \tag{2.10a}$$

$$\vec{u} = \frac{1}{\rho}\sum_{k=1,8} \vec{e}_k f_k, \tag{2.10b}$$

$$T = \frac{1}{\rho}\sum_{k=0,8} g_k, \qquad \text{(for model I)}, \tag{2.10c}$$

$$T = \sum_{k=1,4} g_k, \qquad \text{(for model II)}. \tag{2.10d}$$

Under the small Mach number assumption, these quantities are the solutions of the conservation equations

$$\nabla \vec{u} = 0, \tag{2.11a}$$

$$\frac{\partial \vec{u}}{\partial t} + \nabla(\vec{u} \cdot \vec{u}) = -\frac{1}{\rho}\nabla p + \nu \nabla S + \vec{F}, \tag{2.11b}$$

$$\frac{\partial T}{\partial t} + \nabla \cdot (\vec{u}T) = \alpha \nabla^2 T, \tag{2.11c}$$

where

$$S_{ij} = \frac{1}{2}\Big(\frac{\partial u_i}{\partial x_j} + \frac{\partial u_j}{\partial x_i}\Big),$$

is the strain rate tensor, which can be computed simply using the non-equilibrium part of the density distribution function Eq. (2.12), in contrast to velocity derivations in classical methods

$$S_{ij} = -\frac{3}{2\rho\tau_f}\sum_k \vec{e}_{ki}\vec{e}_{kj}\big(f_k - f_k^{eq}\big). \tag{2.12}$$

Such a form is very useful when implementing turbulence models which will be discussed in the following sections.

3 Code validation

This section is devoted to the code validation. The considered problem is a two dimensional natural convection in a rectangular geometry of height H and width W (see Fig. 2). The cavity is filled with air. The flow in the enclosure is governed by the Navier-Stokes equations under Boussinesq assumption. A horizontal temperature gradient $(T_h - T_c)$ is imposed to the vertical walls and zero flux conditions are applied to the horizontal walls. The no-slip boundary condition reigns on the cavity walls. Under the Boussinesq assumption the forcing term of Eq. (2.4) is written as

$$\vec{F}_k = 3w_k\rho\beta T\vec{g}\cdot\vec{e}_k,$$

where β is the thermal expansion coefficient. Two dimensionless parameters are considered here, i.e., the Prandtl number

$$\mathrm{Pr} = \frac{\nu}{\alpha} = 0.71,$$

and the Rayleigh number

$$Ra = \frac{g\beta(T_h - T_c)H^3}{\nu\alpha}.$$

In the case of a square cavity, H=W, the calculations are presented for $10^5 \leq \mathrm{Ra} \leq 10^6$ in Table 1. The grid sizes are chosen to be 150^2 and 200^2 for $\mathrm{Ra}=10^5$ and 10^6 respectively. The LBM prediction shows a good agreement with published benchmark solutions based on traditional CFD methods for the tested range of Ra number. It is well known that the flow, for $\mathrm{Ra}>10^5$, shows a stretched boundary layers near isothermal walls and a temperature stratification at the core of the cavity. Fig. 3 illustrates the dynamic and thermal structure for $\mathrm{Ra}=10^5$ and 10^6. For further details, readers can refer to [5]. It is shown in [5] that the LBM is two-order accuracy in space and that the $\overline{\mathrm{Nu}} - \mathrm{Ra}$ relation-ship agrees well with the established correlations in the literature. One notes

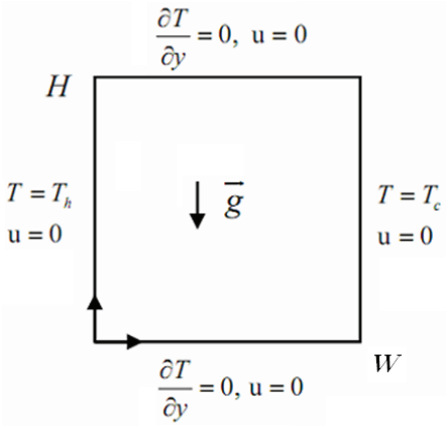

Figure 2: Computational domain and boundary conditions for a natural convection problem.

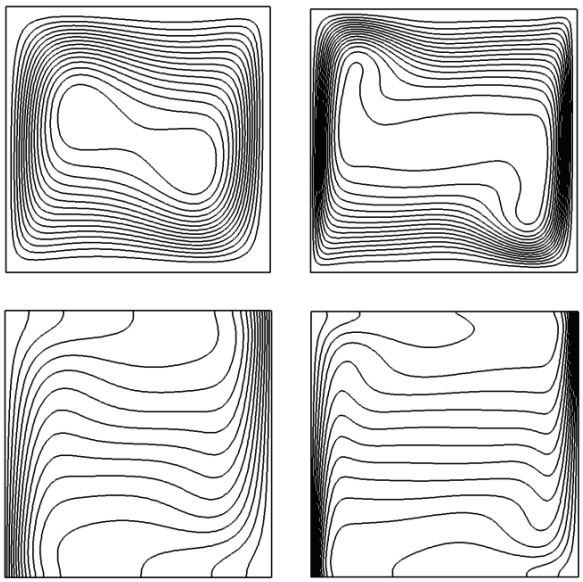

Figure 3: Contour-maps of streamlines (above) and isotherms (below) for Ra=10^5 (left) and Ra=10^6 (right).

here that $\overline{\mathrm{Nu}}$ is the averaged Nusselt number computed as

$$\overline{\mathrm{Nu}} = \frac{1}{\alpha \Delta T/H} \frac{1}{H^2} \int_0^H \int_0^H \left[uT - \alpha \left(\frac{\partial T}{\partial x} \right) \right] dxdy. \tag{3.1}$$

As the onset of time-dependent flow in a cavity occurs at earlier Rayleigh numbers in Rayleigh-Bénard configuration than in a cavity with adiabatic horizontal walls, we perform a computation for a Rayleigh-Bénard configuration with aspect ratio W/H=2. The flow structure changes continuously with time (see [24]) characterizing the onset of time-dependent flow. The time-history of hot wall Nusselt number and its energy spectrum are illustrated in Fig. 4. The primary dimensionless frequency for the LB prediction is close to 15.86, the Finite Volume prediction gives 15.81 (in unit of H^2/α), which confirms the high level of predictability for the LB approach.

Table 1: Comparison of present results with results of references [22, 23].

Ra		$\mathrm{U}_{\max}$	y	$\mathrm{V}_{\max}$	x	$\overline{\mathrm{Nu}}$
10^5	Model I	34.7475	0.8533	68.5756	0.0667	4.4887
	Model II	34.7171	0.8533	68.4794	0.0667	4.4926
	[22]	34.722	0.855	68.590	0.066	4.519
	[23]	34.736	0.855	68.640	0.065	4.523
10^6	Model I	65.2202	0.8500	220.5421	0.0399	8.7533
	Model II	65.2238	0.8500	220.2941	0.0399	8.7639
	[22]	64.630	0.850	219.360	0.0379	8.800
	[23]	64.775	0.850	220.640	0.0350	8.800

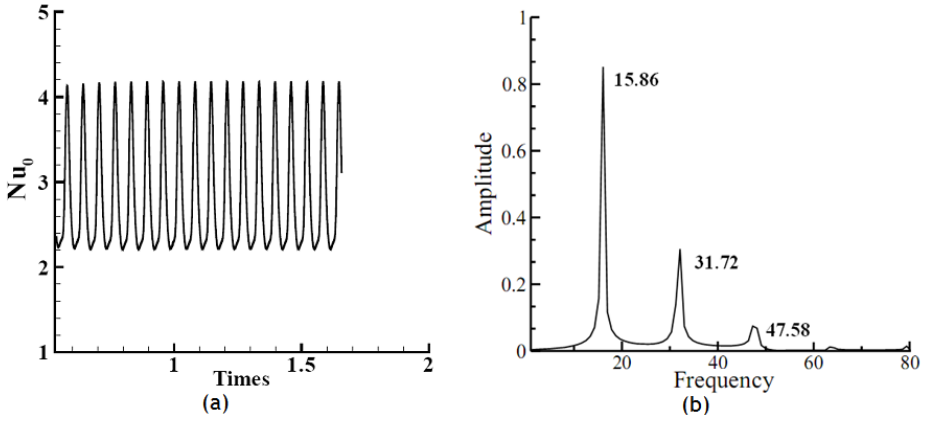

Figure 4: Time history of hot-wall Nusselt number (a) and its spectra of amplitude frequency (b).

4 Numerical results and discussions

4.1 Transitions thresholds for low Prandtl number flows in enclosures

Phase change is of major interest in crystal growth processes. Low Prandtl flows in cavities subjected to temperature gradients fall into these categories. Thus, there have been many efforts to understand the occurring phenomena in such flows, since a high control permits high quality pure crystals in one side and stable dynamic solutions permits qualifying the critical operating parameters of crystal growth in other side. Therefore, the investigation of stability for these types' flows is of great importance for practical applications. In this part we consider two situations with symmetry breaking for low Prandtl number flowing in enclosures. In these two cases the routes to unsteadiness are investigated using the thermal LB model I. The present results are expressed in terms of Grashof number (Gr=Ra/Pr) for the seeking of comparison with previous ones. The reference scales for length, time, velocity and pressure are respectively H, H^2/α, α/H and $\rho(\alpha/H)^2$ and the dimensionless temperature is written as

$$\theta = \frac{T - T_c}{T_h - T_c}.$$

For the classical vertical Bridgman cavity, the simplified model is depicted in Fig. 5, the Prandtl number is chosen to be 0.01 and the resolution is taken 200×200. The onset of the flow results from the Rayleigh-Bénard configuration. For low values of Gr number, the flow is a steady symmetric structure (SS) characterized by two counter-rotating cells. With the increase of Gr, the thermal transfer is enhanced and the flow becomes slightly asymmetric (SAS) for Gr=2.5 10^5, where the stream-function magnitude is close to 0.3786. However, its value for Gr=3 10^5, is of 0.3517, then the stream-function magnitude reaches its maximum in this Grashof number range. This critical value is located at about $Gr_c \approx 2.75\ 10^5$ and indicates a change in the flow pattern characterized

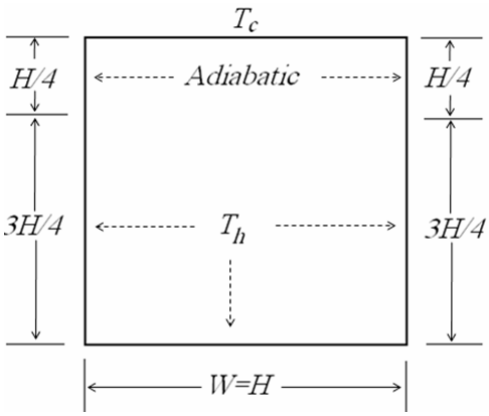

Figure 5: Simplified vertical Bridgman configuration with fixed interface.

by a typical symmetry breaking in the melt flow structure (see Fig. 5). This behaviour confirmed by the 2D Spectral results [25] where transition threshold is identified between 2.5 10^5 and 3 10^5 and 3D FV ones [26]. A comparative table recapitulates each result gathered to the used method (see Table 2).

With more increase of Grashof number, the flow becomes steady and absolutely asymmetric (SAS). Moreover, we observe the growth progressively of the left roll and the reduction of the right one. For Gr=6 10^5, the flow structure is completely dominated by one roll slightly distorted by the presence of two small left-vortices and the two-linked right-vortices.

The two-linked right-vortices are reduced for Gr about 10^6 and the flow remains steady dominated by one cell formed by perfect circles centred at the cavity centre until Gr=17 10^5. However, the up-right vortices disappear since Gr=14 10^5 marking a new flow regime in the too-next Grashof numbers. Two others tested values of Gr (17.5 10^5, 17.75 10^5) give a time-dependent state. The stream-function magnitude decreases much and the flow becomes periodic (P1) for Gr=17.9 10^5, with a dimensionless frequency f_c=7.033 which agrees well with the FV results (f_c=6.67) obtained by [27], the transition thresholds of the two results are close to the Spectral and 3D Finites Volumes ones.

For the horizontal Bridgman cavity, the resolution is taken 400 × 100 in a shallow configuration with aspect ratio A=4 (see Fig. 7). The cavity is filled with Gallium of

Table 2: Thresholds transitions in vertical Bridgman growth for Pr=0.01.

Method	Symmetric Gr = 2 10^5 $\psi_{\max}$	Transition SS-SAS Gr	Transition SAS-P1 Gr(f_c)
Spectral [25]	-	2.5-3 10^5	20 10^5
FV (3D) [26]	-	3 10^5	-
FV (2D) [27]	0.290	3.50 10^5	17.5 10^5 (6.670)
LBM (2D) [33]	0.308	2.75 10^5	17.9 10^5 (7.033)

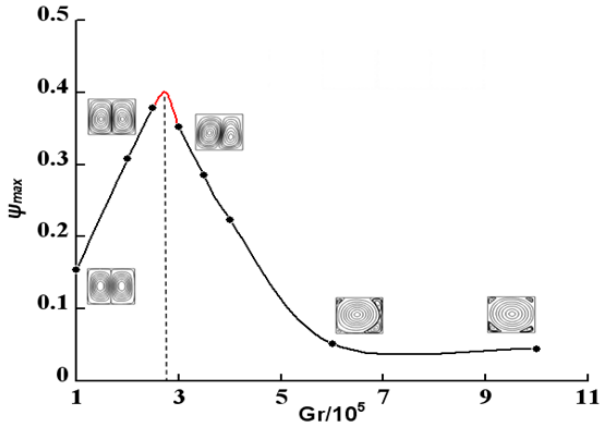

Figure 6: Threshold transition diagram for the vertical Bridgman model.

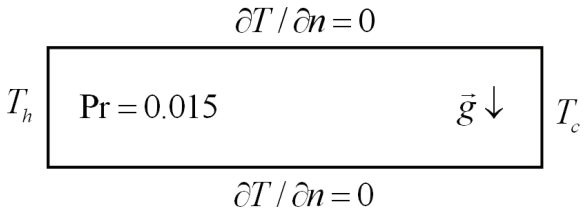

Figure 7: Simplified horizontal Bridgman configuration with fixed interface.

Prandtl number 0.015. The simplified model considers a fixed interface maintaining at constant temperature as for former established benchmarks.

For Gr=5000, the flow is a one convective clock-wise rotating cell. A transition occurs at a critical value of $Gr \approx 32000$ and the flow structure is a three counter-rotating cells. The present results are gathered to previous solutions [28–32] in Table 3 and the bifurcations diagram defined by the plot of maximum stream-function magnitude vs the Grashof number is established (see Fig. 8). In the vicinity of the critical point the Grashof number is increased uniformly (by a step of 250). For Gr=32250, the flow exhibits a three cells structure. However, for Gr=32500 a new transition characterized by two-cell structure is identified. The regime remains steady again with two rolls until Gr=33330. For Gr=40000, a change in the cells-shape is observed near isothermal walls, the stream-function magnitude increases considerably and no time dependency is remarked. This behaviour defines a new branch with two cells in the flow patterns which have been investigated in [27].

Further details of the two cases can be found in [32]. One can conclude that LBM

Table 3: Symmetry breaking, Hopf point estimated with various methods, A=4 and Pr=0.015.

Method	FDM [28]	Spectral [29]	FEM [30,31]	FVM [32]	Spectral [32]	LBM [33]
Mesh	121 × 41	40 × 30	66 × 24	60 × 24	200 × 100	400 × 100
Gr	32500-33500	33300	33002	32500-33500	32996	32000

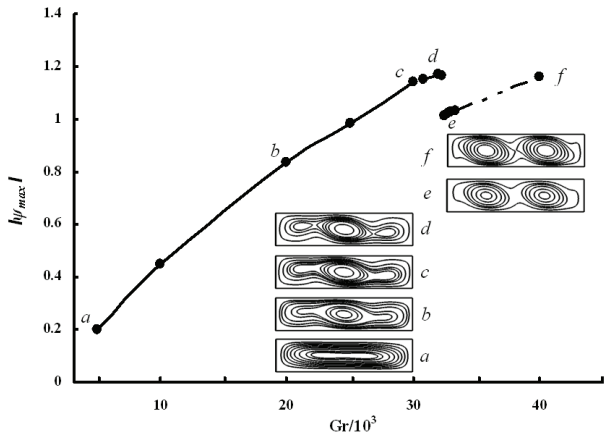

Figure 8: Bifurcation diagram for the horizontal Bridgman model (fixed interface) for Pr=0.015.

results are in excellent agreement with those in previous works and LBM can predict accurately the threshold of transition in horizontal and vertical Bridgman growth as the traditional methods in CFD.

4.2 Porous media flows in enclosures under external magnetic force

This section will offer a general idea devoted to explore an extended thermal lattice Boltzmann model simulating flows under complex conditions (configuration, external forces, $\cdots$,). The results of the numerical examples demonstrate the potential of the LBM to deal with this kind of problems.

The LBM has been successfully applied to simulation of porous media flows [34]. The force due to the presence of porous media as well as the other external forces is taken into account by introducing an added term into the Navier-Stokes equations. Thanks to its simplicity, the forcing terms, which are linear or non-linear can be simply appended to the Boltzmann equation collision term. Moreover, the macroscopic velocity can be deduced by a simple quadratic form (see [34]). In the case of natural convection flow in porous media subjected to external magnetic force, the external force term becomes more complex. It includes porous media effects (linear and non-linear drag terms), the gravitational force and the magnetic force,

$$F_i = \varepsilon g_i \beta (T_c - T) - \frac{\varepsilon \nu}{\kappa} u_i - \varepsilon F_\varepsilon \sqrt{\frac{u_i u_i}{\kappa}} u_i + \varepsilon \sigma \left[(B_j u_j) B_i - B^2 u_i \right], \qquad i = 1, 2, \tag{4.1}$$

where ε is the medium porosity, κ is the medium permeability, F_ε is a geometric parameter; σ is the fluid electric conductivity and B is the magnetic field magnitude.

As mentioned in [35], the forcing term in LBE can take different forms and all forms give similar results. In the following, we'll keep the same form which is given above. The cavity inclination and the magnetic field direction are controlled respectively by

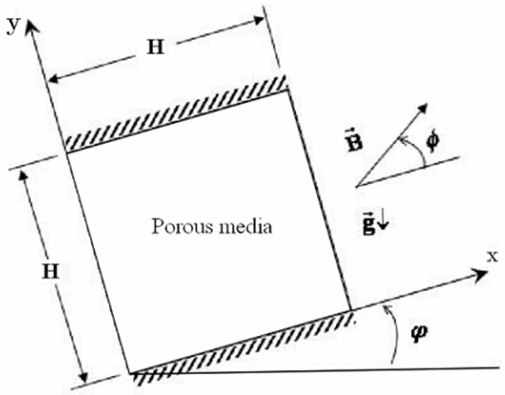

Figure 9: Schematic illustration of natural convection problem for fluid flowing into inclined porous media and subjected to inclined magnetic field.

the angles φ and ϕ (see Fig. 9). Hence,

$$\vec{g} = g\big(\cos(\varphi), \sin(\varphi)\big), \qquad \vec{B} = B\big(\cos(\phi), \sin(\phi)\big),$$

see [34] and [36] for further details. The boundary conditions are the same as the configuration of Fig. 2. The flow is monitored by the Rayleigh number, the Darcy number, the medium porosity and the Hartman number. The Prandtl number is kept 0.71. The thermal model II indicated above is used here. The steady state convergence is accelerated by using the procedure used in [37]. The kinetic viscosity is taken 0.01, 0.007 and 0.003 for Ra$\sim\mathcal{O}(10^3)$-$\mathcal{O}(10^4)$, $\mathcal{O}(10^5)$-$\mathcal{O}(10^6)$ and $\mathcal{O}(10^7)$ respectively. In all the computations, we use the lattice sizes 50×50, 75×75, 100×100, 125×125 and 150×150 for the Rayleigh numbers 10^3, 10^4, 10^5, 10^6 and 10^7 (respectively).

The LBM is firstly applied to solve two test problems, namely a free fluid flow subjected to vertical uniform magnetic field, i.e.,

$$\vec{B} = -|B|\vec{y},$$

and a porous media flow. For both problems φ=0. For the first case, the results are gathered to the Pulicani's ones using the ADI method (see Table 4). The two methods show a good agreement for low Grashof numbers and low Hartman numbers. With the increase of these two parameters, a considerable deviation is remarked. A test result is made by using the Finite Volume method to check the justness of the LB

Table 4: Comparison of the average Nusselt number at the hot wall $\overline{\mathrm{Nu}_0}$ with Ref. [36] for Pr=0.733 in the presence of magnetic field († denotes our results).

Ha	10			50			100		
Gr	LBM†	FVM†	ADI	LBM†	FVM†	ADI	LBM†	FVM†	ADI
2.10^4	2.2780	2.2976	2.2234	1.0900	1.1154	1.0856	1.0177	1.0113	1.0110
2.10^5	5.0518	4.9865	4.8053	3.0784	3.2901	2.8442	1.4866	1.6430	1.4317
2.10^6	9.8852	9,7904	8.6463	8.9326	9.0563	7.5825	6.7142	7.2416	5.5415

Table 5: Comparison of the average Nusselt number with Ref. [34] for Pr=1.

		$\varepsilon = 0.4$		$\varepsilon = 0.6$	
Da	Ra	Present	[34]	Present	[34]
10^{-4}	10^5	1.066	1.067	1.072	1.071
	10^6	2.595	2.550	2.711	2.725
	10^7	7.816	7.810	8.532	8.183
10^{-2}	10^3	1.008	1.010	1.013	1.015
	10^4	1.360	1.408	1.491	1.530
	10^5	2.989	2.983	3.435	3.555

results. The FV results show an excellent agreement with the LB ones. The deviation of the ADI method may be attributed to the coarser grid size used.

For the fluid flowing in porous media, a comparison is done based on the averaged Nusselt number within the cavity for different Rayleigh numbers, Darcy numbers and medium porosities. A good agreement is obtained compared with previous works (see Table 5).

It is worth pointing out that from the two benchmarks established by evaluating the heat transfer rate (average Nusselt number), the present LBM (model II) can be efficiently used for simulation of flows for various combinations of these parameters. The effects of the variations of the Rayleigh number and the cavity inclination are investigated with setting ϕ=0°, Ha=50, ε=0.4 and Da=10^{-2}. As shown in Fig. 10, increasing the Rayleigh number or the cavity inclination affects strongly the dynamic and thermal field's structures in the presence of the external magnetic force in the porous media. For φ=0°, increasing the buoyancy force (Ra) enhances the convective currents dumped (or suppressed) by the magnetic force effect for low Rayleigh numbers. The isotherms become stretched near the isothermal walls and equally spaced at the cavity core. For φ=90°, the flow pattern becomes more complex due to the Rayleigh-Bénard phenomenon. Furthermore, for φ=90°, a pair and two pairs counter-rotating cells are formed for (respectively) Ra=10^5 and 10^6, compared with free fluid flow in enclosures.

The effects of the Darcy number and the medium porosity are also examined for Ra=10^5, φ=0°, Ha=50 and ϕ=0°. The flow structure is for all a single counter clockwise rotating cell. As for the previous investigation, the effects of the Darcy number and the medium porosity are significant. By decreasing the Darcy number (logarithmically), the infiltration velocity in the medium decreases considerably, the thermal behavior tends to take a conductive mode signature. The presence of the magnetic field results in decreasing the heat transfer compared with the case of flow in porous media without external force and forming in somewhat a diagonal-acting region as shown in Fig. 11. At the same time, increasing the medium porosity enhances slightly the convective currents near the insulated walls firstly resulting in a small rotation of the isotherms and diagonally-extended elliptic cell at the core and secondly with a tendency to have the well-known horizontal stratified thermal structure.

The study of the effects of varying the Hartmann number and the magnetic field inclination (taking Ra=10^5, φ=0°, Da=10^{-2} and ε=0.4) show that: (i) increasing the

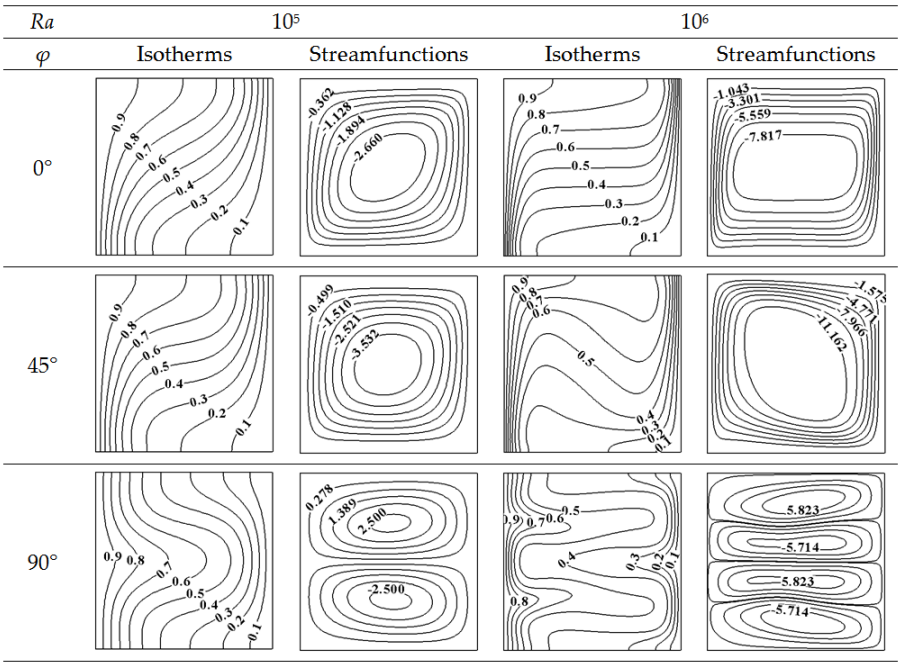

Figure 10: Contour maps of isotherms and iso-streamfunction for Pr=1, Da=10^{-2}, ε=0.4, Ha=50 and ϕ=0°.

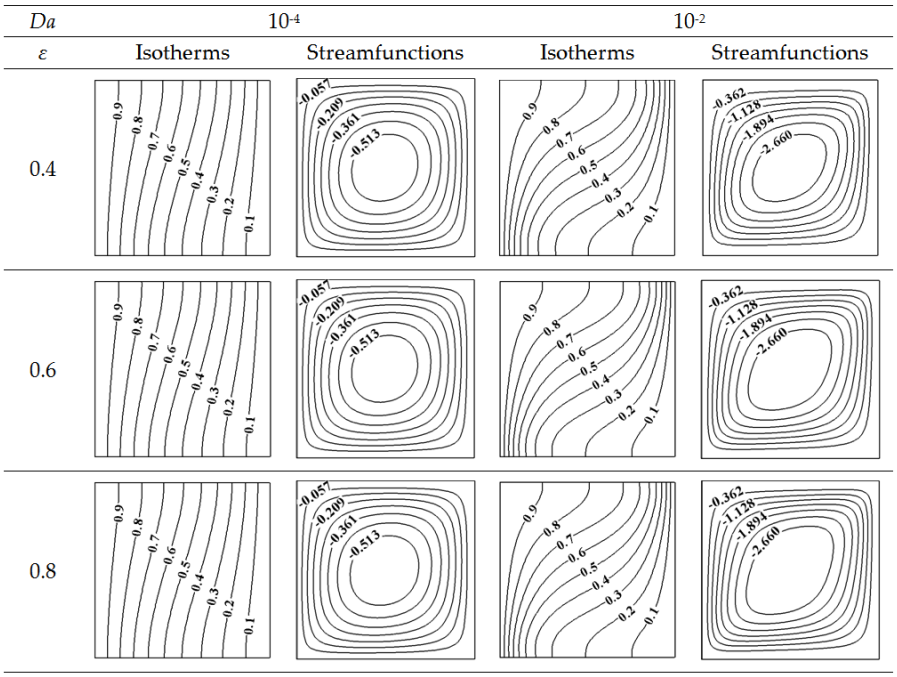

Figure 11: Contour maps of isotherms and iso-streamfunction for Ra=10^5, φ=0°, Pr=1, Ha=50 and ϕ=0°.

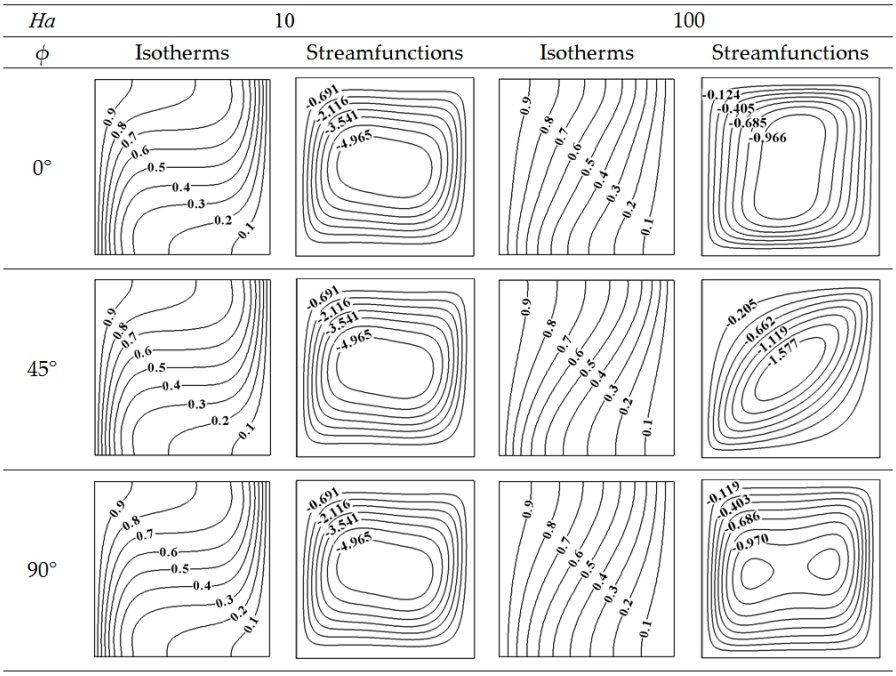

Figure 12: Contour maps of isotherms and iso-streamfunction for Ra=10^5, φ=0°, Pr=1, Da=10^{-2} and ε=0.4.

Hartmann number changes considerably the flow and thermal behaviors, (ii) the dynamic structure is indifferent to the variation of magnetic field inclination but it expresses a major dependency for high Hartman number. For Ha=100, when the magnetic field is applied in "$x+$" direction the central eddy is extended in the vertical direction (see Fig. 12); when the magnetic field is applied diagonally, the dynamic structure becomes more extended diagonally; and when the magnetic field is applied in the "$y+$" direction, the dynamic central eddy becomes extended horizontally and two small vortices appear in the core region. However, the thermal structure (iii) it seems to be indifferent to the magnetic field inclination for this Hartman number range. For Ha=10, the buoyancy force dominates the magnetic force and the isotherms show a near-horizontal-stratification. With more increase of the Hartman number, the isotherms become equally spaced yielding to a diagonal thermal stratification.

4.3 Axisymmetric plasma jet flows

This part deals with the investigation of plasma jets using an axisymmetric LB thermal model. Plasma jets have been very successful in many applications (such as spraying, cutting, welding, $\cdots$,). The excellent choice of high performance plasma gases and spraying materials has been the subject of several experimental and numerical efforts. An excellent choice will be the response of efficient numerical studies and the results of experimental tests. Plasma jets are a high temperature flows (>8000K). Therefore, all

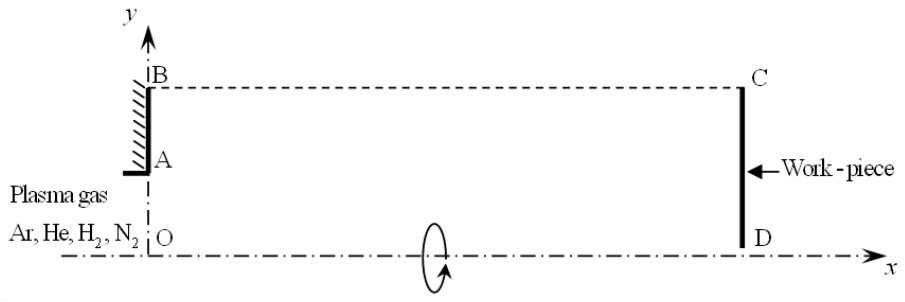

Figure 13: Computational domain.

diffusion parameters involved in conservation equations are temperature dependent. In the following we present a plasma jet investigation in an axisymmetric LBM (Jian's model [38]). In the context of our knowledge, it is the first intend to tackle this field by using the LBM. Further reading on solution procedure, the model implementation and assumptions may be found in [39,40]. The thermal model II will be adopted here.

A half plan is considered as a computational domain for the axisymmetric plasma jet. The graph is mapped in Fig. 13. The plasma gas used is the argon issuing into argon surrounding. OA (=R=4mm) is the torch radius, AB (=11*OA) is the anode thickness considered to be isothermal solid boundary ($\mathbf{u}$=0, T=$T_{\min}$), BC is a free boundary ($\partial\Phi/\partial y$=0, Φ=$\mathbf{u}$ or T), OD (=L=100mm) is the axisymmetric axis and CD will be decided afterwards. The domain is a 97×201 lattice nodes.

The inlet profiles at the edge OA are expressed as

$$\begin{cases} u_{in} = u_{\max}\left\{1 - \left(\dfrac{y}{R}\right)^3\right\}, \\ T_{in} = \left(T_{\max} - T_{\min}\right)\left[1 - \left(\dfrac{y}{R}\right)^4\right] + T_{\min}, \end{cases} \tag{4.2}$$

where

$$u_{\max} = 520\text{m/s}, \quad T_{\max} = 13500\text{K} \quad \text{and} \quad T_{\min} = 700\text{K}.$$

One way is used to account for the temperature dependent parameters. One obtains the same value when adimensionalizing a quantity Φ in LB space and the Physical (real) space as

$$\frac{\Phi_{LB}}{LB\_scale} = \frac{\Phi_{Ph}}{Ph\_scale}, \tag{4.3}$$

which leads to

$$\Phi_{LB} = \Phi_{Ph}\frac{LB\_scale}{Ph\_scale}. \tag{4.4}$$

The plasma jet is laminar in its core but turbulent in its fringes due to the high field gradients (200 K/mm and 10 m/s/mm). In LBM-LES modelling of turbulence, only the collision relaxation time is locally readjusted, by adding the eddy viscosity v_t to the molecular one as:

$$\tau_{f\_tot} = 3\nu_{tot} + 0.5 = 3(\nu + \nu_t) + 0.5 = 3\left[\nu + (C_{smag}\Delta)^2|S_{ij}|\right] + 0.5, \tag{4.5}$$

where C_{smag} is the Smagorinsky constant, Δ is filter width (=1) and $|S_{ij}|$ is the strain rate tensor defined in Eq. (2.12). Eq. (4.5) yields to a quadratic equation in τ_{f_tot} that leads to

$$\tau_{f\_tot}(x,t) = \frac{1}{2}\left\{\tau_f + \left[\tau_f^2 + 18\frac{(C_{smag}\Delta)^2|Q_{ij}|}{\rho(x,t)}\right]^{\frac{1}{2}}\right\}, \tag{4.6}$$

where

$$Q_{ij} = \sum_k e_{ki}e_{kj}(f_k - f_k^{eq}) \quad \text{and} \quad |Q_{ij}| = \sqrt{2Q_{ij}Q_{ij}}.$$

Similarly for the thermal field, the relaxation time is readjusted by using the new thermal diffusivity as:

$$\alpha_{tot} = \frac{\tau_{g\_tot} - 0.5}{2} = \alpha + \alpha_t = \alpha + \frac{\upsilon_t}{\mathrm{Pr}_t}, \tag{4.7}$$

where Pr_t is the turbulent Prandtl number usually taken between 0.3 and 1.

First of all, a validation analysis based on free jet is done. Therefore, the boundary CD is considered as a free boundary. The present LB results based on the centreline axial-velocity (Fig. 14) and temperature (Fig. 15) are compared with Pfender's numerical and experimental results [41] and the results of the Jets & Poudres ones [42] for specified jet conditions (see [39]).

One can remark that the axial temperature gradient near the inlet (interval 0-25 mm) is close to 220 K/mm then close to 200 K/mm observed experimentally (counter 136 K/mm and 152 K/mm for Jet & Poudres and Pfender results respectively) and the velocity gradient is close to 8.8 (m/s)/mm (counter 10.48 (m/s)/mm and 9.48 (m/s)/mm for Jet & Poudres and Pfender results respectively), which agree well with former experimental and numerical observations as noted here-above. It is also clear that our results go well with Jet & Poudres ones. The disparity between the two results in the potential core of the plasma jet (hot zone) is probably due to the fact that ramps are used in Jet & Poudres code for the inlet temperature and velocity profiles instead

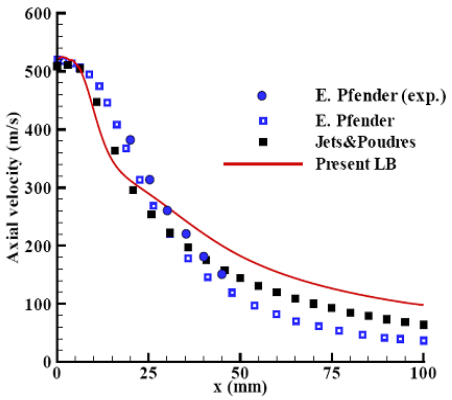

Figure 14: Centerline-axial velocity distribution simulated on a LBGK D2Q9 lattice with $C_{smag} = 0.18$ and $\mathrm{Pr}_t = 0.3$ in comparison with referenced results.

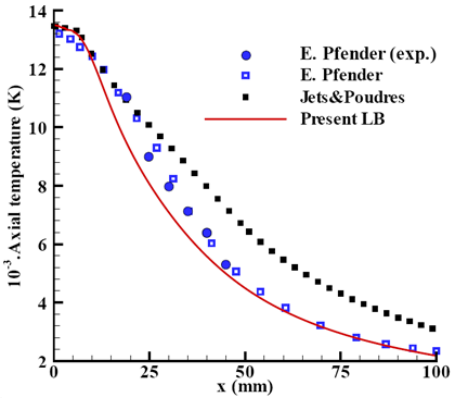

Figure 15: Centerline-temperature distribution simulated on a LBGK D2Q9 lattice with $C_{smag} = 0.18$ and $\mathrm{Pr}_t = 0.3$ in comparison with referenced results.

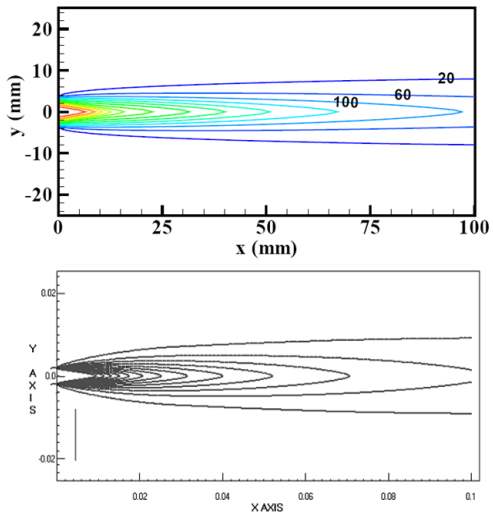

Figure 16: Axial-velocity distributions for *Jets & Poudres* code (below) and LBGK (above), outer-line 20 m/s and 40 m/s for interval.

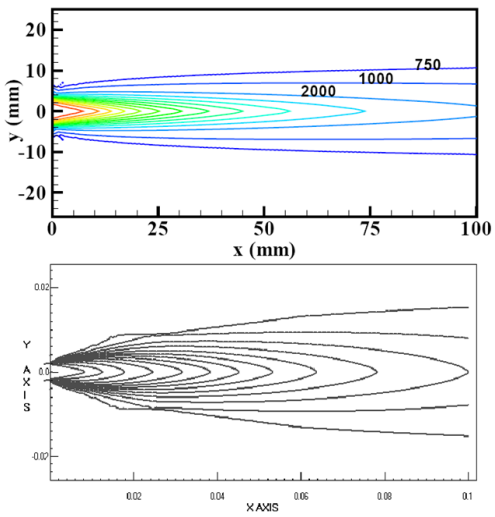

Figure 17: Temperature distributions for *Jets & Poudres* code (below) and LBGK (above) with 1000K for outer-line and interval.

of ours parabolic ones. After that, in the plasma jet core, the profiles become Gaussian and the two curves go together.

Figs. 16 and 17 present the isotherms and iso-axial velocities of our results and those of Jets & Poudres. It is clear from LB results that the temperature distribution is more expanded than the axial-velocity one and it shares this characteristic with the Finite-Difference (Jet & Poudres) results. One can also say that Jets & Poudres jet is more expanded and that our results are consistent with the most previous predicted results [43] where the jet width does not exceed at all 10 mm for the temperature and velocity distributions. This behaviour, for LB results, is in good agreement with experimental plasma-jet characteristics because plasma jet is more extended, however Jet & Poudres results are more representative for flame jet which is more expanded.

Fig. 18 shows the radial temperature distributions at different distances from the nozzle exit. The Gaussian profile holds for all the cross sections. The maximum axial temperature decreases with increasing the axial distance and Gaussian profile becomes more flattened.

With more increase of the maximum inlet velocity, results in a considerable translation of the velocity fringes and a small translation of the isotherms ones. An important issue in plasma jets modelling is to take account for the target (substrate) as a fixed boundary condition. Consequently, the flow and thermal structures will change. The idea is very intuitive for a good (real) prediction of dynamic and thermal history of in-flight particles. The work-piece may have several inclinations with plasma jet axe. The impinging angle is one of several parameters controlling the manner in which a molten or semi-molten particle flattens and solidifies. We just consider here the case of plasma jet impinging normally on the work-piece. The non-slip boundary condition

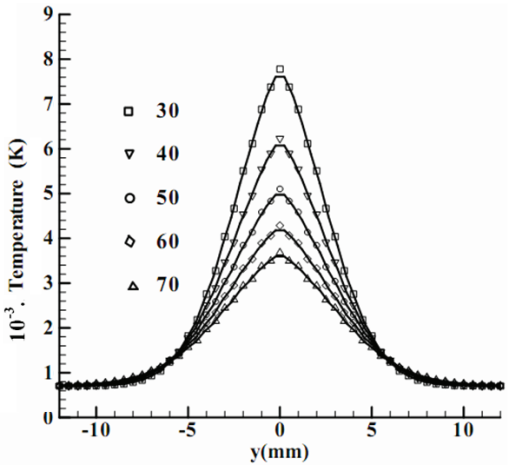

Figure 18: Radial temperature distribution for different cross sections simulated on a LBGK.

and low temperature are retained in our treatment. The target stands 100 mm away from the torch exit. Results are depicted in Figs. 19 and 20.

Distributions in Figs. 19 and 20 are in good agreement with the literature results [43]. The temperature and the axial velocity distributions are flatten locally at the down stream near the work piece. The centreline fields' profiles undergo major variations. The deformation of the jet near work-piece will affect appreciably the sprayed particles trajectories and heating history and particularly its incidence.

Through this pure argon test case, the LBM is found to be able to describe efficiently the plasma jet behaviour. However, in plasma spraying it is of great importance to choose the appropriate plasma gas for the spraying material. Then, the mixture gases are used when looking for some jet properties that depend on the volume rates. The LBM has been used in [40] to simulate a mixture of gases, namely the N2-Ar62.5% vol. The LB results are compared with the Jets & Poudres and GENMIX [42] ones for the same characteristics discussed above for pure argon plasma. A good agreement is found with the two codes using different turbulence models.

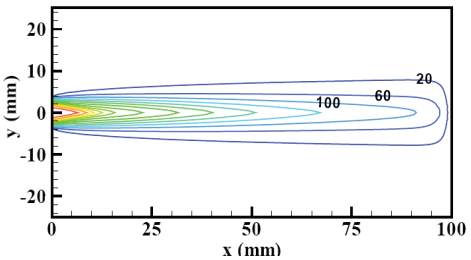

Figure 19: Axial-velocity distribution for a jet impinging normally on the substrate, outer-line 20 m/s and 40 m/s for interval.

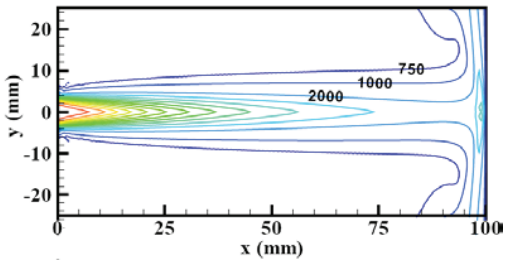

Figure 20: Temperature distribution for a jet impinging normally on the substrate with 1000 K for outer-line and interval.

5 Conclusions

The paper reviews some critical advances in the lattice Boltzmann modelling and simulations for complex thermal flows. It illustrates the developments based on selected application examples. These examples are not only tested cases for the LBM approach but they also form a large number of problems of major interest in industry. On the basis of these LBM numerical studies, the following conclusions can be drawn:

1. The computed results demonstrate that LBM has a good ability to captivate flow bifurcation thresholds. Particularly cavities exhibiting bifurcation sequences are considered and the results are consistent with prior observations,
2. The lattice Boltzmann method exhibits an excellent flexibility to deal with complex flows and shows a high degree of predictability compared with traditional method in CFD,
3. The simplicity and accuracy of the method are at the head of its exceptional advantages. It is important to describe accurately the complex fluid flow and interface deformations in a realistic configuration (3D without simplified models) for the first two cases studies. For the plasma jet case study, a good representation of the plasma jet physics results in a good interaction between plasma and in-flight particles (dynamic and heat transfers) and consequently a good agreement with measured results. These fields will be the subjects of our future works.

References

[1] S. CHEN AND G. D. DOOLEN, *Lattice Boltzmann method for fluid flows*, Ann. Rev. Fluid. Mech., 30 (1998), pp. 329–364.
[2] Z. GUO, B. SHI AND C. ZHENG, *A coupled lattice BGK model for the Boussinesq equations*, Int. J. Num. Meth. Fluids., 39 (2002), pp. 325–342.
[3] X. SHAN AND H. CHEN, *Lattice Boltzmann model for simulating flows with multiple phases and components*, Phys. Rev. E., 47 (1993), pp. 1815–1819.
[4] C. M. TEIXEIRA, *Incorporating turbulence models into the Lattice-Boltzmann method*, Int. J. Mod. Phys. C., 9 (1998), pp. 1159–1175.
[5] R. DJEBALI, M. EL GANAOUI, H. SAMMOUDA AND R. BENNACER, *Some benchmarks of a side wall heated cavity using lattice Boltzmann approach*, FDMP, 164(1) (2009), pp. 1–21.
[6] Y. PENG, C. SHU AND Y. T. CHEW, *A 3D incompressible thermal lattice Boltzmann model and its application to simulate natural convection in a cubic cavity*, J. Comput. Phys., 193 (2003), pp. 260–274.
[7] Z. L. GUO AND T. S. ZHAO, *A lattice Boltzmann thermal model for convection heat transfer in porous media*, Numer. Heat. Trans. B., 47(2) (2005), pp. 157–177.
[8] Y. PENG, C. SHU AND Y. T. CHEW, *Simplified thermal lattice Boltzmann model for incompressible thermal flows*, Phys. Rev. E., 68 (2003), 026701.
[9] A. A. MOHAMAD, M. EL-GANAOUI AND R. BENNACER, *Lattice Boltzmann simulation of natural convection in an open ended cavity*, Int. J. Therm. Sci., 48(10) (2009), pp. 1870–1875.
[10] M. A. MOUSSAOUI, M. JAMI, A. MEZRHAB AND H. NAJI, *MRT-Lattice Boltzmann simulation of forced convection in a plane channel with an inclined square cylinder*, Int. J. Therm. Sci., 49(1) (2010), pp. 131–142.

[11] E. SEMMA, M. EL GANAOUI, R. BENNACER AND A. A. MOHAMAD, *Investigation of flows in solidification by using the lattice Boltzmann method*, Int. J. Therm. Sci., 47 (2008), pp. 201–208.
[12] E. A. SEMMA, M. EL GANAOUI AND R. BENNACER, *Lattice Boltzmann method for melting/solidification problems*, Comptes Rendus Mécanique, 335(5-6) (2007), pp. 295–303.
[13] L. P. WANG, B. ROSA, H. GAO, GUOWEI HE AND G. JIN, *Turbulent collision of inertial particles: point-particle based, hybrid simulations and beyond*, Int. J. Multiphase. Flow., 35 (2009), pp. 854–867.
[14] H. XU, W. TAOA AND Y. ZHANG, *Lattice Boltzmann model for three-dimensional decaying homogeneous isotropic turbulence*, Phys. Lett. A., 373 (2009), pp. 1368–1373.
[15] H. N. DIXIT AND V. BABU, *Simulation of high Rayleigh number natural convection in a square cavity using the lattice Boltzmann method*, Int. J. Heat. Mass. Trans., 49(3-4) (2006), pp. 727–739.
[16] Y. PENG, C.SHU, Y. T. CHEW AND J. QIU, *Numerical investigation of flows in Czochralski crystal growth by an axisymmetric lattice Boltzmann method*, J. Comput. Phys., 186 (2003), pp. 295–307.
[17] A. A. MOHAMAD, *Lattice Boltzmann method for heat diffusion in axis-symmetric geometries*, Pro. Comput. Fluid. Dyn., 9(8) (2009), pp. 490–494.
[18] L. ZHENG, B. SHI, Z. GUO AND C. ZHENG, *Lattice Boltzmann equation for axisymmetric thermal flows*, Comput. Fluids., 39 (2010), pp. 945–952.
[19] J. G. ZHOU, *Axisymmetric lattice Boltzmann method*, Phys. Rev. E., 78 (2008), 036701.
[20] G. MULLER, G. NEUMANN AND W. WEBER, *Natural convection in vertical Bridgman configuration*, J. Crystal. Growth., 70 (1984), pp. 78–93.
[21] A. A. MOHAMMAD, Applied Lattice Boltzmann Method for Transport Phenomena Momentum Heat and Mass Transfer, The University of Calgary Press, 2007.
[22] G. DE VAHL DAVIS, *Natural convection of air in a square cavity: a benchmark numerical solutions*, Int. J. Numer. Methods. Fluids., 3 (1983), pp. 249–264.
[23] C. SHU AND H. XUE, *Comparison of two approaches for implementing stream function boundary conditions in DQ simulation of natural convection in a square cavity*, Int. J. Heat. Fluid. Flow., 19 (1998), pp. 59–68.
[24] R. DJEBALI, M. EL GANAOUI AND H. SAMMOUDA, *Investigation of a side wall heated cavity by using lattice Boltzmann method*, Euro. J. Comput. Mech., 18 (2009), pp. 217–238.
[25] P. LARROUDÉ, J. OUAZZANI, L. I. D. ALEXANDER AND P. BONTOUX, *Symmetry breaking flow transitions and oscillatory flows in a 2D directional solidification model*, Euro. J. Mech. B., 13(3) (1994), pp. 353–381.
[26] R. BENNACER, M. EL GANAOUI AND E. LEONARDI, *Symmetry breaking of melt flow typically encountered in a Bridgman configuration heated from below*, Appl. Math. Model., 30 (2006), pp. 1249–1261.
[27] A. SEMMA, Etude Numérique des Transferts de Chaleur et de Masse Durant la Croissance Dirigée : Effet de Paramètres de Contrôle, Thèse de Doctorat de L'école Mohammadia D'Ingénieurs, Université Mohamed V, Maroc, 2004.
[28] H. BEN HADID AND B. ROUX, *Buoyancy-driven oscillatory flows in shallow cavities filled with low-Prandtl number fluids*, In Proc. GAMM Workshop on Numerical Solution of Oscillatory Convection in Low Prandtl Number Fluids (ed. B. Roux), Notes on Numerical Fluid Mechanics, 27 (1990), pp. 25–33, Vieweg, Braunschweig.
[29] P. PULICANI, A. CRESPO DEL ARCO, A. RANDRIAMAMPIANINA, P. BONTOUX AND R.PEYRET, *Spectral simulations of oscillatory convection at low Prandtl number*, Int. J. Numer. Methods. Fluids., 10 (1990), pp. 481–517.

[30] K. H. WINTERS, *Oscillatory convection in liquid metals in a horizontal temperature gradient*, Int. J. Numer. Methods. Engng., 25 (1988), pp. 401–414.
[31] K. H. WINTERS, *A bifurcation analysis of oscillatory convection in liquid metals*, Proc. GAMM Workshop on Numerical Solution of Oscillatory Convection in Low Prandtl Number Fluids (ed. B. Roux), Notes on Numerical Fluid Mechanics, 27 (1990), pp. 319–326, Vieweg, Braunschweig.
[32] A. Y. GELFGAT, P. Z. BAR-YOSEPH AND A. L. YARIN, *Stability of multiple steady states of convection in laterally heated cavities*, J. Fluid. Mech., 388 (1999), pp. 315–334.
[33] M. EL GANAOUI AND R. DJEBALI, *Aptitude of a Lattice Boltzmann method for evaluating transitional thresholds for low Prandtl number flows in enclosures*, C.R. Mécanique, 338 (2010), pp. 385–396.
[34] Z. GUO AND T. S. ZHAO, *A lattice Boltzmann model for convection heat transfer in porous media*, Numer. Heat. Trans. B., 47 (2005), pp. 157–177.
[35] A. A. MOHAMAD AND A. KUZMIN, *A critical evaluation of force term in lattice Boltzmann method, natural convection problem*, Int. J. Heat. Mass. Trans., 53 (2010), pp. 990–996.
[36] N. RUDRAIAH, R M. BARRON, M. VENKATACHALAPPA AND C. K. SUBBARAY, *Effect of a magnetic field on free convection in a rectangular enclosure*, Int. J. Engng. Sci., 33(8) (1995), pp. 1075–1084.
[37] K. N. PREMNATH, M. J. PATTISON AND S. BANERJEE, *Steady state convergence acceleration of the generalized lattice Boltzmann equation with forcing term through preconditioning*, J. Comput. Phys., 228 (2009), pp. 746–769.
[38] J. G. ZHOU, *Axisymmetric lattice Boltzmann method*, Phys. Rev. E., 78 (2008), 036701.
[39] R. DJEBALI, B. PATEYRON, M. EL GANAOUI AND H. SAMMOUDA, *Axisymmetric high temperature jet behaviors based on a lattice Boltzmann computational method: part I. argon plasma*, Int. Rev. Chem. Eng., 1(5) (2009), pp. 428–438.
[40] R. DJEBALI, B. PATEYRON, M. EL GANAOUI AND H. SAMMOUDA, *Lattice Boltzmann computation of plasma jet behaviors: part II. argon-azote mixture*, Int. Rev. Chem. Eng., 2(1) (2010), pp. 86–94.
[41] E. PFENDER AND C. H. CHANG, *Plasma spray jets and plasma-particulates interactions: modeling and experiments*, Proceeding of the 15th International Thermal Spray Conference, 25-29, May 1998, Nice, France.
[42] 'Jets & Poudres' free downlowd from `http://www.unilim.fr/spcts` or `http://jets.poudres.free.fr`.
[43] D. Y. XU, X. C. WU AND X. CHEN, *Motion and heating of non-spherical particles in a plasma jet*, Surf. Coat. Tech., 171 (2003), pp. 149–156.